ENVISAT/AATSR derived land surface temperature over a heterogeneous region

Guillem Sòria, José A. Sobrino *

Global Change Unit, Department of Thermodynamics, Faculty of Physics, University of Valencia, Burjassot, Spain

Abstract

In this paper a method for evaluating land surface temperature (LST) algorithms over heterogeneous areas is presented. The evaluation was made for a set of 12 algorithms derived by using the split-window (SW) and dual-angle (DA) techniques for estimating sea and land surface temperature (SST and LST) from Advanced Along-Track Scanning Radiometer (AATSR) data. A validation of the proposed algorithms was carried out over a heterogeneous region of Morocco in the framework of the WATERMED (WATer use Efficiency in natural vegetation and agricultural areas by Remote sensing in the MEDiterranean basin) project. AATSR data and in situ measurements over this heterogenous region were compared by implementing a classification based strategy over a higher spatial resolution Landsat image. Three reference classes were considered when performing the classification from the Landsat image. Ground based measurements where then used to assign an effective surface radiometric temperature to each of these three classes. Finally, an averaging procedure based on class proportion was implemented for deriving surface radiometric temperature at the AATSR pixel scale. For this heterogeneous site, the results showed that LST can be obtained with a root mean-square error (RMSE) lower than 1.7 K from the split-window algorithms. Dual-angle algorithms, on the other hand, provided greater RMSE due to the different surfaces observed in the nadir and forward views. The results suggest that to retrieve LST from 1 km pixels over heterogeneous surfaces spatial averaging is required to improve accuracy on temperature estimation.
© 2007 Elsevier Inc. All rights reserved.

Keywords: Land surface temperature; Heterogeneity; Spatial variability; Split-window; Dual-angle; AATSR; Remote sensing

1. Introduction

The measurement of Land Surface Temperature (LST) is of considerable importance for environmental studies on regional and global scales (Barton, 1992; Lagouarde et al., 1995; Schmugge et al., 2002). The surface temperature is an input parameter needed in the study of the fluxes at the surface–atmosphere interface. The retrieval of land surface temperature has additional difficulties in comparison with the sea surface. This is mainly due to the large heterogeneity of the land surface because of the vegetation, topography and soil physical properties.

In spite of these difficulties, several theoretical studies successfully developed LST algorithms applicable to different sensors as AVHRR, Thematic Mapper, MODIS, ASTER and the ATSR series through the split-window (SW) method (Becker & Li, 1990; Prata, 1993; Price, 1984; Sobrino et al., 1991, 1994, 1999, etc.). On the other hand, making use of the multiangular viewing capability present on the (A)ATSR series of sensors, LST was also retrieved from these sensors by using the dual-angle (DA) method (Sobrino et al., 1996, 2004).

The SW method uses observations at two different spectral bands within the 10–12 μm spectral region, to remove atmospheric effects. The benefit of the SW method over this spectral range is based upon large spectral variations of the atmospheric absorption, as compared to surface emissivity. The DA method uses observation with the same channel but from two different angles, to exploit the effect of different absorption path lengths. Both methods to developed LST algorithms are usually calibrated over radiative transfer code simulations. The main error source in these calibrations is the spectral parameterization of the atmospheric absorption due to the water vapor continuum. Therefore, the coefficients from the split-

* Corresponding author. Dr Moliner 50 — 46100 Burjassot, Valencia, Spain. Tel./fax: +34 96 354 3115.

E-mail address: sobrino@uv.es (J.A. Sobrino).

window algorithm are affected by a double error, one for each channel, and depend strongly on the transmission code used (Grant, 1990). However, this is not the case for the DA method: it relies on angular variations of atmospheric transmission and emission, and therefore allows minimizing spectral inaccuracies inherent to the parameterization of radiative transfer codes. This confirms the theoretical advantage of the DA method as compared to the SW method, if the spectral and angular variations of emissivity are of the same order of magnitude (Chédin et al., 1982). Sobrino et al. (1996) concluded that DA technique is capable of producing Sea Surface Temperature (SST) with an RMSE of less than 0.23 K if the satellite data are error free. They also showed that when the spectral and angular variations of emissivity are of the same order, the DA method provides a better behavior than the SW one. However, estimating LST with DA technique requires precise knowledge of angular variation of the surface emissivity.

The DA method can be made from simultaneously measuring from different satellites e.g. Meteosat and TIROS-N (Chédin et al., 1982), or from a single satellite. Currently, the only observing system able to provide quasi-simultaneous multispectral measurements at two view angles is the Advanced Along-Track Scanning Radiometer (AATSR) sensor. The 1st of March 2002, the European Space Agency (ESA) mission ENVISAT (ENVIronment SATellite) was launched, with the AATSR onboard. As its predecessor sensors from the ATSR series, it includes a special dual-angular feature. Each point of the Earth's surface is observed twice: first in a forward swath (inclined path through the atmosphere) and after 120 s, in a nadir swath. View zenith angle ranges from 0° to 21.6° in nadir viewing, and from 52.4° to 55° in forward viewing. Each observation angle has a different pixel field-of-view (IFOV) at the center of the swath. Pixel size in the nadir view is 1 km by 1 km, but 1.5 km by 2 km in the forward view. The sensor has 7 bands in the visible, near and thermal infrared, with central wavelengths at 0.56, 0.66, 0.86, 1.6, 3.7, 10.9 and 12.1 μm.

The AATSR was initially designed to provide sea surface temperature (SST) maps. However nowadays AATSR data is being used more and more to obtain LST on a global scale. A Level 2-LST product is currently provided by ESA according to the AATSR Algorithm Theoretical Basis Document (Prata, 2002). The algorithms proposed to produce the Level 2-LST images of the AATSR sensor use pixel-by-pixel top-of-the-atmosphere cloud-free, calibrated and navigated day and night brightness temperatures from the 11 and 12 μm AATSR channels. This algorithm also requires as inputs the following parameters: seasonally-dependent land cover classification, fractional vegetation and precipitable water. the first two were determined using the biomes provided by Dorman and Sellers (1989) from a grid of 1°×1° resolution. The precipitable water data is based on the NVAP climatology at 2.5°×2.5° resolution and monthly intervals. This spatial resolution for both fractional cover and precipitable water is currently one of the main problems in the retrieval of the LST.

Recent studies (Jia et al., 2003) show the interest of angular measurements with satellite observations in the separation of soil and vegetation temperatures. LST requires additional considerations as compared to SST products, because of larger heterogeneities. Besides, land surface emissivities are much more variable than sea surface ones. If emissivity and atmospheric effects are not correctly accounted for, errors up to more than 12 K may result in the retrieving of LST (Becker, 1987), (Sobrino & Raissouni, 2000) and (Sobrino et al., 2003). Most of the papers that report validations of LST products only deal with homogeneous surfaces. For example, Sobrino et al. (2004) showed the good behavior of SW and DA ATSR-2 algorithms over a homogeneous region of Australia. In the case of non-homogeneous surfaces, the retrieval of LST on a per-pixel basis strongly depends on the spatial resolution of the pixels compared. Since DA technique applied to AATSR data makes use of two different pixel size images, it has a greater impact than the SW technique that uses images with the same spatial resolution. Therefore, it is necessary to extend the validation exercises over heterogeneous land surfaces.

According to the previously mentioned, this paper has two main aims:

a) to provide a series of new SW and DA algorithms for the retrieval of LST from AATSR data. The set of algorithms would include a different amount of parameters according to the availability of input data.
b) to validate the proposed algorithms over a heterogeneous region by implementing a classification based strategy over a higher spatial resolution image.

2. Theory and algorithms

The structure of the theoretical algorithms was obtained from the radiative transfer equation, considering the at-sensor radiance ($L_\lambda^{\text{at-sensor}}$) for a given wavelength (λ) as:

$$L_{\lambda\theta}^{\text{at-sensor}} = [\varepsilon_{\lambda\theta}B(\lambda, T_s) + (1 - \varepsilon_{\lambda\theta})L_\lambda^{\text{atm}\downarrow}]\tau_{\lambda\theta} + L_{\lambda\theta}^{\text{atm}\uparrow} \qquad (1)$$

where $\varepsilon_{\lambda\theta}$ is the surface emissivity, $B(\lambda, T_s)$ is the radiance emitted by a blackbody (BB) at temperature T_s of the surface, $L_\lambda^{\text{atm}\downarrow}$ is the hemispherical downwelling radiance, $\tau_{\lambda\theta}$ is the total atmospheric transmittance and $L_{\lambda\theta}^{\text{atm}\uparrow}$ is the upwelling atmospheric radiance. All these variables also depend on the observation angle θ.

In general, the terms referring to the downwelling and upwelling sky radiance are very complex. For simplicity, and according to Sobrino et al. (1996), we assumed that the sky radiance is isotropic, the surface and the atmosphere are in local thermodynamic equilibrium and we used Kirchhoff's law to express the directional reflectivity of the surface in terms of directional emissivity. From these considerations, the upwelling and downwelling atmospheric radiance can be substituted, respectively, by:

$$L_{\lambda\theta}^{\text{atm}\uparrow} = (1 - \tau_{i\theta})B_\lambda(T_a) \qquad (2)$$

$$L_\lambda^{\text{atm}\downarrow} = (1 - \tau_{i53})B_\lambda(T_a) \qquad (3)$$

where T_a is the effective mean atmospheric temperature and τ_{i53} is the total atmospheric path transmittance at 53°.

In order to compare both dual-angle and split-window algorithms in the retrieving of surface radiometric temperature, the same mathematical structure for both methods was used. In fact, Sobrino et al. (1996) showed that the choice of the same mathematical structure for both the dual-angle and split-window algorithms can be based on two considerations: an adequate inter-comparison between both SW and DA methods, and due to the fact that the base of an atmospheric correction algorithm in the thermal infrared can be the differential absorption between two different bands. Indeed, the same difference in atmospheric absorption can be obtained by simultaneous measurements at two different wavelengths, and by measurements at the same wavelength but from different angles. This can be verified as the atmospheric transmittance of the 12 μm channel at nadir view and the 11 μm channel with a view angle of 53° are equivalent as a function of the total water vapor content at nadir.

Thus, substituting both atmospheric radiance Eqs. (3) and (4) in the radiative transfer Eq. (1), an algorithm involving temperatures can be obtained using a first-order Taylor series expansion of the Planck's law and writing the equation for i and j (i and j being two different channels observed at the same angle, SW method, or the same channel with two different observation angles, DA method):

$$T_s = T_i + A_0(T_i - T_j) - A_1 + A_2(1 - \varepsilon) - A_3\Delta\varepsilon_\theta \qquad (4)$$

where A_0 to A_3 are coefficients that depend on atmospheric transmittances, ε is the mean value of the emissivities over channels i and j (in the case of SW method) or the emissivity of channel i (DA method), $\Delta\varepsilon_\theta$ is the spectral variation (SW method) or angular variation (DA method) of the emissivity, T_i and T_j are the brightness temperatures for two different channels with the same view angle, SW method, or for the same channel with two different view angles, DA method, in accordance with Sobrino et al. (2004). Using Eq. (4) we can obtain a separation between the atmospheric and emissivity effects in the retrieval of surface radiometric temperature.

The calibration of the dual-angle and split-window coefficients was made using MODTRAN radiative transfer code (Abreu & Anderson, 1996; Berk et al., 1998) simulations for 60 different radiosoundings. These radiosoundings were extracted from the TOVS initial guess retrieval (TIGR) data base (Scott & Chedin, 1981). The brightness temperatures were calculated for a large range of near surface temperature gradient. It consisted of five surface temperatures $T-5$, T, $T+5$, $T+10$, and $T+20$, where T is the first boundary layer temperature of the atmosphere. The variation of the zenith angle in a nadir image is from 0° to 21.6°, and from 52.4° to 55° in the forward image. The variation of the atmospheric path absorption, due mainly to the presence of water vapor, can be characterized by an angular function. This function has some principal angles (Gaussian angles) that are well determined (Wan & Dozier, 1989). According to the range of variation of the AATSR images, four view zenith angles (0°, 11.2°, 24.7°, and 53.8°) were used.

Furthermore, 9 different emissivity spectra were obtained from the Salisbury and D'Aria (1992) library, which includes several types of surfaces (grass, dry grass, conifers, deciduous, sea, sand (2 types), and mud (2 types)). These types of surfaces chosen are representative of the 90% of the Earth's landcover. The AATSR waveband emissivities were obtained by integration of the response functions with the appropriate emissivity spectrum. Angular dependence of surface emissivities was taken into account. The emissivities for channels at forward view were calculated using the factors defined by: Labed and Stoll (1991), Sobrino and Cuenca (1999) and McAtee et al. (2003). These factors give a relation between emissivities at nadir view (0° to 21.6°) and forward view (52° to 55°). As a result, we had 10,800 different geophysical situations (60 atmospheres, 5 temperatures, 4 angles and 9 types of surfaces). The emissivities calculated can be observed in Fig. 1, with a range from 0.91 to 0.99. In general, emissivities at 12 μm are greater than those at 11 μm, whereas different angular decreasing are observed according to the considered sample. The atmospheric water vapor at nadir was extracted from the 60 radiosoundings of the TIGR database, providing a range of $(0–5)$ g cm^{-2} for the simulations.

A set of 24 different structures were considered for the proposed algorithms, 12 for the SW method (6 at nadir view and 6 at forward view) and 12 for the DA method (6 using 11 μm spectral band and 6 using 12 μm spectral band. These algorithms have different dependencies on the input parameters: the linear difference of brightness temperature $(T_i - T_j)$, quadratic difference of brightness temperature (quad, $(T_i - T_j)^2$), water vapor content (W), emissivity (ε) and spectral or angular emissivity difference ($\Delta\varepsilon$ or $\Delta\varepsilon_\theta$). Once the different structures of the algorithms were determined, the Levenberg–Marquardt method was used to minimize them. This method is a non-linear least-squares algorithm, being a robust and efficient modification of the Gauss–Newton method. An analysis of the method can be found in Moré (1997) and Press et al. (1989).

Error theory was applied to all of the algorithms studied.

- The residual atmospheric error, σ_{mod}, is related to the accuracy in surface radiometric temperature determination.
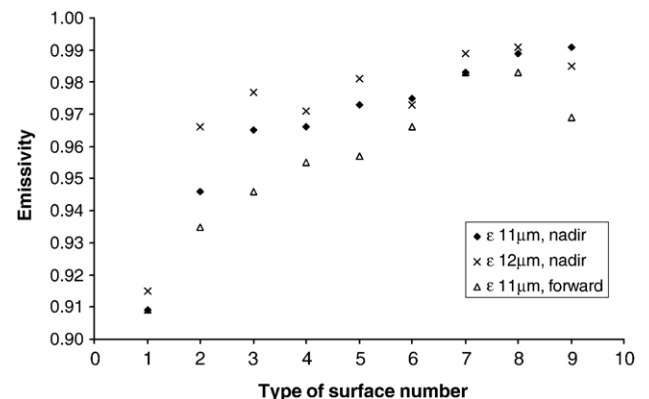

Fig. 1. Emissivities in nadir (0°) and forward (55°) views for the surface types considered in the simulation (1: Dry grass, 2: Mud1, 3: Sand 1, 4: Mud2, 5: Sand 2, 6: Deciduous, 7: Grass, 8: Conifers, 9: Sea).

Table 1a
Numerical coefficients and standard deviation for the split-window algorithms proposed

Name	Expression	σ_{mod} (K)	σ_{noise} (K)	σ_ε (K)	σ_{WV} (K)	σ_{total} (K)
SW1 n: quad	$T_s = T_{2n} + 0.61(T_{2n} - T_{1n}) + 0.31(T_{2n} - T_{1n})^2 + 1.92$	1.73	0.07	–	–	1.73
SW2 n: quad, ε	$T_s = T_{2n} + 0.76(T_{2n} - T_{1n}) + 0.30(T_{2n} - T_{1n})^2 + 0.10 + 51.2(1 - \varepsilon)$	1.39	0.07	0.18	–	1.40
SW3 n: quad, ε, $\Delta\varepsilon$	$T_s = T_{2n} + 1.03(T_{2n} - T_{1n}) + 0.26(T_{2n} - T_{1n})^2 - 0.11 + 45.23(1 - \varepsilon) - 79.95\Delta\varepsilon$	1.05	0.09	0.59	–	1.20
SW4 n: (W), ε, $\Delta\varepsilon$, W	$T_s = T_{2n} + (1.01 + 0.53W)(T_{2n} - T_{1n}) + (0.4 - 0.85W) + (63.4 - 7.01W)(1 - \varepsilon) - (111 - 17.6W)\Delta\varepsilon$	0.59	0.10	0.83	0.45	1.12
SW5 n: quad, ε, $\Delta\varepsilon$, W	$T_s = T_{2n} + 1.35(T_{2n} - T_{1n}) + 0.22(T_{2n} - T_{1n})^2 - (0.82 - 0.15W) + (62.6 - 7.2W)(1 - \varepsilon) - (144 - 26.3W)\Delta\varepsilon$	0.93	0.11	1.06	0.20	1.43
SW6 n: quad (W), ε, $\Delta\varepsilon$, W	$T_s = T_{2n} + (1.97 + 0.2W)(T_{2n} - T_{1n}) - (0.26 - 0.08W)(T_{2n} - T_{1n})^2 + (0.02 - 0.67W) + (64.5 - 7.35W)(1 - \varepsilon) - (119 - 20.4W)\Delta\varepsilon$	0.52	0.15	0.89	0.37	1.10
SW1 f: quad:	$T_s = T_{2f} + 0.43(T_{2f} - T_{1f}) + 0.45(T_{2f} - T_{1f})^2 + 1.79$	2.41	0.06	–	–	2.41
SW2 f: quad, ε:	$T_s = T_{2f} + 0.49(T_{2f} - T_{1f}) + 0.44(T_{11f} - T_{1f})^2 + 0.33 + 33.46(1 - \varepsilon)$	2.31	0.06	0.12	–	2.31
SW3 f: quad, ε, $\Delta\varepsilon$:	$T_s = T_{2f} + 0.70(T_{2f} - T_{1f}) + 0.42(T_{2f} - T_{1f})^2 - 0.004 + 32.89(1 - \varepsilon) - 76.51\Delta\varepsilon$	2.13	0.07	0.55	–	2.20
SW4 f: (W), ε, $\Delta\varepsilon$, W:	$T_s = T_{2f} + (0.55 + 1.03W)(T_{2f} - T_{1f}) + (1.03 - 01.91W) + (57.44 - 10.28W)(1 - \varepsilon) - (111 - 22.1W)\Delta\varepsilon$	1.26	0.10	0.83	0.99	1.80
SW5 f: quad, ε, $\Delta\varepsilon$, W:	$T_s = T_{2f} + 0.4(T_{2f} - T_{1f}) + 0.43(T_{2f} - T_{1f})^2 - (1.4 - 0.9W) + (53.82 - 9.56W)(1 - \varepsilon) - (136 - 28.6W)\Delta\varepsilon$	1.99	0.06	1.01	0.52	2.29
SW6 f: quad (W), ε, $\Delta\varepsilon$, W	$T_s = T_{2f} + (2.41 + 0.3W)(T_{2f} - T_{1f}) - (0.43 - 0.15W)(T_{2f} - T_{1f})^2 + (0.02 - 1.36W) + (60.39 - 11.1W)(1 - \varepsilon) - (128.78 - 27.7W)\Delta\varepsilon$	1.12	0.18	0.96	0.73	1.65

T_{1n}, T_{1f}, T_{2n} and T_{2f} are the brightness temperature of the spectral bands centered on 12 μm and 11 μm at nadir (n) and forward (f) views, respectively.
W is the atmospheric water vapor content. ε is the mean spectral emissivity of channels 12 μm and 11 μm, $\Delta\varepsilon$ is the spectral variation of the emissivity. σ_{mod}, σ_{noise}, σ_ε, σ_{WV}, σ_{total} are, respectively, the standard deviation related to the calibration residual atmospheric uncertainty, the radiometric noise, the uncertainty in the value of the emissivity, the associated with the water vapor column determination and the total error.

This error is the RMSE obtained from both the radiative transfer code inaccuracies and the fitting process;

- The error of the signal acquired by the sensor (σ_{noise}) assumes a noise temperature (NEΔT) of 0.05 K for the AATSR channels (Smith et al., 2001). To compute σ_{noise}, a typical value of the water vapor content of $W = 1$ g cm^{-2} for dry summer atmospheres was used;
- The error associated with the water vapor column determination (σ_W), consider a water vapor content uncertainty of 0.5 g cm^{-2} (Sobrino et al., 1994). Some representative values of brightness temperature and emissivity were needed to compute this standard deviation. The values chosen for the emissivities correspond to a set of values of different soils and crops from the lowest value of 0.950 (for an inceptisol soil) and from the highest value of 0.990 (for conifers);
- The standard deviation associated with the uncertainty in the value of the emissivity (σ_ε) is set at 0.005 (Caselles & Sobrino, 1989).

The total error was calculated, considering the different errors independently, as $\sigma_{\text{total}} = \sqrt{(\sigma_{\text{mod}})^2 + (\sigma_{\text{noise}})^2 + (\sigma_{\text{WV}})^2 + (\sigma_\varepsilon)^2}$.

Tables 1a and b show the algorithms proposed (SW and DA, respectively), where T_{1n}, T_{1f}, T_{2n} and T_{2f} are the brightness temperature of the spectral bands centered on 12 μm and 11 μm at nadir (n) and forward (f) views, respectively. The algorithms are ranked according to their explicit dependence on the input parameters.

Tables 1a and b show that the calibration residual standard deviation is smaller when the algorithm has more degrees of freedom. Besides, dual-angle algorithms give better accuracy than the split-window ones with the same mathematical structure. This fact can be explained by taking into account that the main error source in radiative transfer codes is the spectral parameterization of the atmospheric absorption due to the water vapor continuum. Hence, when a simulation procedure is carried out to obtain a split-window algorithm, a double error is involved, one for each channel (wavelengths of 11 μm and 12 μm). Instead, dual-angle algorithms only consider the error for one thermal channel, i.e., for one wavelength. There is one interesting aspect of the values given in Tables 1a and b; the water vapor dependent algorithms give better results than the other ones, even after including the effect of uncertainty in water vapor content. According to the observations reported by Jacob et al. (2004), the dominant atmospheric effect when observing hot surfaces is absorption by water vapor. Therefore, the explicit inclusion of water vapor within an algorithm must lead to an improvement in the LST retrieval. The results are quite similar for both dual-angle and split-window models when the simplest algorithm (less input parameters) is considered, however the differences increase when increasing the input parameters (see, for instance, algorithm type 6, where SW standard deviation doubles the DA one).

As the aim of this paper is to compare SW and DA performances over heterogeneous areas, only the SW nadir and the DA 11 μm algorithms, that provide lower theoretical standard deviations, were used in the validation process.

3. Methodology: area description and data pre-processing

In order to validate LST algorithms, it has usually been carried out in situ measurements in homogeneous surfaces (Sobrino et al., 2004). In the present paper, for the first time, AATSR LST algorithms are applied over a heterogeneous region. This requires the implementation of new validation strategies.

3.1. Area of study

An intensive series of field experiments was developed in Morocco from the 3rd to the 17th of March, 2003. This field experiment was included in the WATERMED project whose description is given by Sobrino et al. (2001). Measurements of emissivity and surface radiometric temperature were carried out concurrently with the AATSR overpass. The study area where the experimental field campaign took place was located between 31°39′ and 31°41′ N latitude and between 7°33′ and 7°38′ W longitude, on the River Tensift basin in the east of

Marrakech (Morocco), 600 m above sea level. It is characterized by hot and dry summers and short winter seasons with short rainfall periods, and a low water vapor content atmosphere. Therefore there is a reduced probability of clouds. Apart from the grazing lands and bare soil, the area is composed of field crops (mainly barley and wheat) typically of 400 × 100 m in size. Due to the size of the field crops, the area is relatively heterogeneous on the scale of an AATSR pixel (1 km × 1 km).

In order to evaluate the algorithms the area was divided in different classes (Fig. 2). The consideration of three different classes was mainly due to availability of three ground sensors for simultaneous measurements with the AATSR overpass. The first class, named BS, corresponds to bare soil; the second one, named M, to a mixture site of sparse vegetation of barley and bare soil, and finally, the third one, named VG, corresponds to an area of barley.

3.2. Ground experimental setup

Thermal and photometric instrumentation were used in the field, for brightness temperature and atmospheric water vapor content, respectively. All radiometers were calibrated with a calibration source (black body) before and after the measurements. Both brightness temperature and emissivity were measures over the three different classes defined previously, with single band and multi bands thermal radiometers. These radiometers were also used with the box method for emissivity measurements. Atmospheric water vapor content was retrieved with photometers in a place free of obstacles like trees or buildings that might disturb the photometric measurements. A description of the thermal and photometric instrumentation used in the experimental campaign, including their accuracy, is listed below.

The CIMEL CE-312 is a radiance-based thermal-infrared radiometer. It was used for brightness temperature measurements over transects and emissivity measurements with the box method. The detector includes one broad-band filter, 8–14 μm, and three narrower filters, 8.2–9.2 μm, 10.5–11.5 μm and 11.5–12.5 μm. This radiometer has an accuracy of ±0.1 K and a Field-of-View of 10° that corresponds to a footprint of 26 cm of diameter for a measurement height of 1.5 m.

The RAYTEK MID LT radiometer is a radiance-based thermal-infrared radiometer with a single band 8–14 μm and an accuracy of 0.5 K. With a Field-of-View of 14° that corresponds to a footprint of 37 cm of diameter, it was used to obtain integrated values in heterogeneous sites.

The EVEREST model 3000.4ZLC is a single band 8–14 μm radiometer with a resolution of 0.1 K, an accuracy of ±0.5 K and a NEΔT of ±0.1 K. The 4° Field-of-View corresponds to a footprint of 10 cm of diameter.

The EVEREST calibration source model 1000 was used to calibrate the radiometers in the field at an ambient temperature. Its operating range is from 0 °C to 60 °C, with a resolution of 0.1 K and an absolute accuracy of 0.3 K over entire range. Therefore, the calibration source GALAI model 204-P, a variable-temperature blackbody was used in laboratory to calibrate the radiometers. This calibration source, whose

Table 1b
As Table 1a for the dual-angle algorithms proposed

Name	Expression	σ_{mod} (K)	σ_{noise} (K)	σ_ε (K)	σ_{WV} (K)	σ_{total} (K)
DA1 (11): quad	$T_s = T_{2n} + 1.36(T_{2n} - T_{2f}) + 0.18(T_{2n} - T_{2f})^2 + 1.78$	1.31	0.11	–	–	1.32
DA2 (11): quad, ε	$T_s = T_{2n} + 1.56(T_{2n} - T_{2f}) + 0.15(T_{2n} - T_{2f})^2 - 0.34 + 51.9(1 - \varepsilon_{2n})$	0.72	0.12	0.18	–	0.75
DA3 (11): quad, ε, $\Delta\varepsilon$	$T_s = T_{2n} + 1.57(T_{2n} - T_{2f}) + 0.15(T_{2n} - T_{2f})^2 - 0.11 + 51.7(1 - \varepsilon_{2n}) - 25.8\Delta\varepsilon_\theta$	0.69	0.13	0.26	–	0.74
DA4 (11): (W), ε, $\Delta\varepsilon$, W	$T_s = T_{2n} + (1.62 + 0.3W)(T_{2n} - T_{2f}) + (0.18 - 0.52W) + (70.1 - 7.18W)(1 - \varepsilon_{2n}) - (35.4 - 3.67W)\Delta\varepsilon_\theta$	0.47	0.13	0.35	0.36	0.70
DA5 (11): quad, ε, $\Delta\varepsilon$, W	$T_s = T_{2n} + 1.92(T_{2n} - T_{2f}) + 0.12(T_{2n} - T_{2f})^2 - (0.39 + 0.09W) + (71 - 7.55W)(1 - \varepsilon_{2n}) - (35.8 - 3.88W)\Delta\varepsilon_\theta$	0.57	0.15	0.36	0.17	0.71
DA6 (11): quad (W), ε, $\Delta\varepsilon$, W	$T_s = T_{2n} + (2.67 - 0.07W)(T_{2n} - T_{2f}) - (0.29 - 0.09W)(T_{2n} - T_{2f})^2 - (0.31 + 0.28W) + (72.5 - 7.9W)(1 - \varepsilon_{2n}) - (35.8 - 4.1W)\Delta\varepsilon_\theta$	0.38	0.20	0.37	0.24	0.62
DA7 (12) quad	$T_s = T_{1n} + 1.25(T_{1n} - T_{1f}) + 0.32(T_{1n} - T_{1f})^2 + 1.79$	1.62	0.12	–	–	1.62
DA8 (12) quad, ε	$T_s = T_{1n} + 1.38(T_{1n} - T_{1f}) + 0.31(T_{1n} - T_{1f})^2 - 0.08 + 47.32(1 - \varepsilon_{1n})$	1.31	0.13	0.17	–	1.33
DA9 (12) quad, ε, $\Delta\varepsilon$	$T_s = T_{1n} + 1.36(T_{1n} - T_{1f}) + 0.31(T_{1n} - T_{1f})^2 - 0.07 + 48.81(1 - \varepsilon_{1n}) - 23.9\Delta\varepsilon_\theta$	1.29	0.13	0.24	–	1.32
DA10 (12) W, ε, $\Delta\varepsilon$, W	$T_s = T_{1n} + (1.51 + 0.65)(T_{1n} - T_{1f}) + (0.74 - 1.3W) + (76.27 - 11.2W)(1 - \varepsilon_{1n}) - (38.76 - 5.76W)\Delta\varepsilon_\theta$	0.85	0.13	0.39	0.82	1.25
DA11 (12) quad, ε, $\Delta\varepsilon$, W	$T_s = T_{1n} + 1.62(T_{1n} - T_{1f}) + 0.28(T_{1n} - T_{1f})^2 - (0.71 - 0.18W) + (76.2 - 11.45W) \times (1 - \varepsilon_{1n}) - (37.85 - 5.8W)\Delta\varepsilon_\theta$	1.25	0.14	0.38	0.22	1.33
DA12 (12) quad (W), ε, $\Delta\varepsilon$, W	$T_s = T_{1n} + (3.46 - 0.06W)(T_{1n} - T_{1f}) - (0.47 - 0.15W)(T_{1n} - T_{1f})^2 - (0.33 + 0.76W) + (81 - 12.6W)(1 - \varepsilon_{1n}) - (42.1 - 6.7W)\Delta\varepsilon_\theta$	0.67	0.27	0.42	0.47	0.96

ε_{1n} and ε_{2n} are the emissivity of the spectral band centered on 12 μm and 11 μm, respectively. $\Delta\varepsilon_\theta$ is the angular variation of the emissivity between nadir and forward views for the spectral band considered.

operating range is from 0 °C to 100 °C, has a sensitivity of 0.1 K and an absolute accuracy of 0.2 K over entire range.

More details about the thermal infrared radiometers are given in Table 2.

A box was also used in the field campaign to obtain absolute emissivity of the classes using the emissivity box method. These emissivity values were used for converting radiometer measurements of brightness temperature into radiometric temperature, to be next used as reference for the validation exercise. References to the emissivity box method can be found in Buettner and Kern (1965), Dana (1969), and Sobrino and Caselles (1993). As a

brief summary, we can describe the box as a bottomless box, the side walls of which are specular reflective surfaces of polished aluminum with a very low emissivity (less than 0.03). The box has two different lids, which can be changed quickly, with different characteristics of absorption and emission. The "cold lid" is a specular reflective cover of polished aluminum. The "hot lid" is a cover of rough aluminum painted using a high emissivity paint (greater than 0.99, Nerry et al., 1990) with internal heating resistances that permit temperatures higher than 373 K. It has a spectral response of an ideal diffusor with a high emissivity.
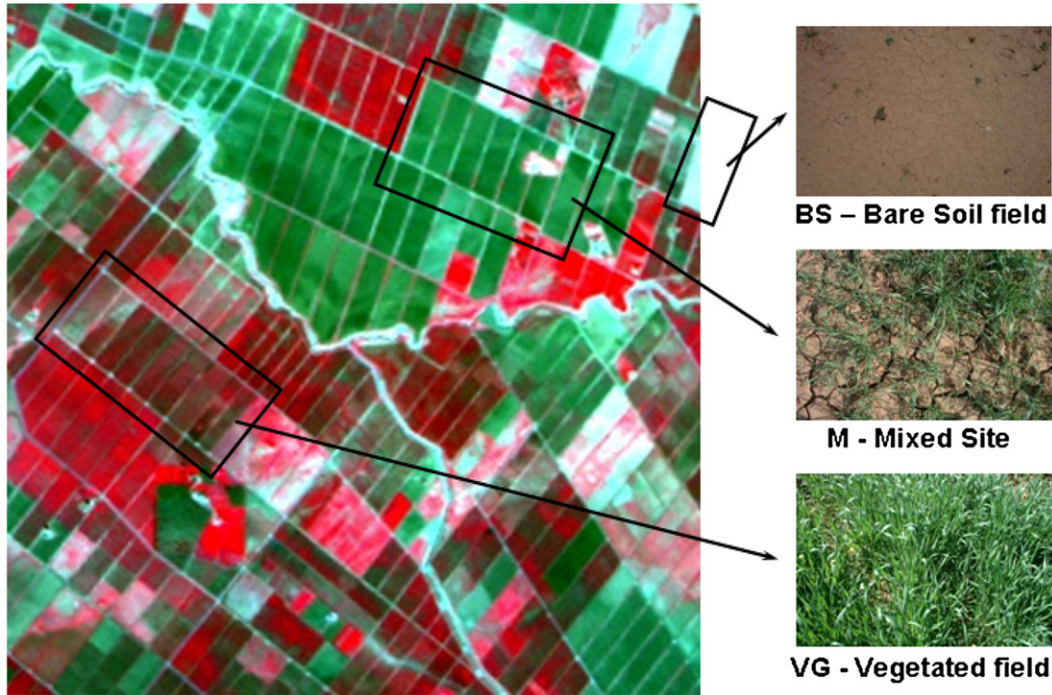
Fig. 2. Merged images of Spot and TM-Landsat 5 of the area of study and samples of the locations.

The MICROTOPS II sensor is a portable photometer which operates with five channels and is capable of directly providing the total ozone content, the water vapor content and the aerosol optical depth at 1020 nm in the whole atmospheric column at nadir. It was used for measuring precipitable water vapor by using a differential absorption between 940 nm and 1020 nm bands. All channels have a collimator with a field of view of 2.5° and deflectors to remove internal reflections. The inaccuracy due to nonlinearity is kept below 0.002% and the combined precision is between 1 and 2% (Estelles et al., 2004; Gómez-Amo et al., 2006; Morys et al., 2001).

3.3. Ground based measurements

3.3.1. Surface radiometric temperature

For our validation exercise, the radiometric temperature obtained from an algorithm is compared with a reconstructed radiometric temperature from ground based brightness temperature. In order to obtain this average surface radiometric temperature of every class, a set of transects were carried out with the different thermal radiometers: the CIMEL radiometer was located in the BS site; the EVEREST transducer was located in the M site, and the RAYTEK MID radiometer at the VG site.

Table 2
Thermal infrared radiometers settings

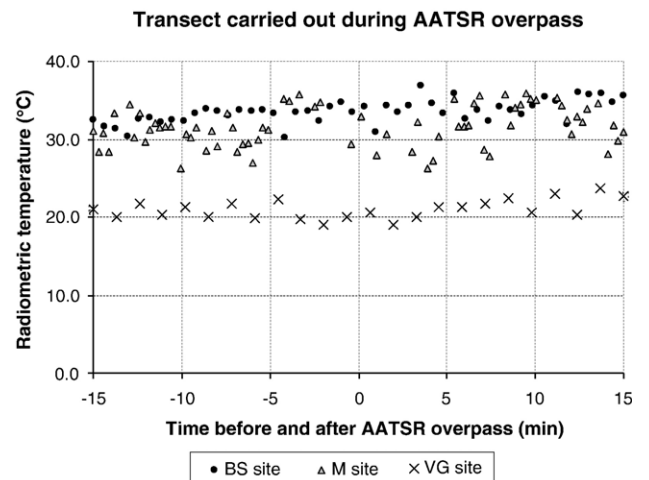| Model	Spectral response (μm)	Temperature range (°C)	Radiometric sensitivity (accuracy) (K)	Field of view (°)
CIMEL CE 312	8–13 8.2–9.2 10.3–11.3 11.5–12.5	−80 to 60	±0.1	10
EVEREST 3000.4ZLC	8–14	−40 to 100	±0.1 (±0.5)	4
RAYTEK MID	8–14	−40 to +600	±0.1 (±1.0)	14
Calibration source: EVEREST 1000		0 to 60	±0.1 (±0.3)	
Calibration source: Galai 204-P		0 to 100	±0.1 (±0.2)	

Fig. 3. Brightness temperature measured in Bare Soil (BS), Mixed (M) and Vegetated (VG) sites measured with CIMEL, EVEREST and RAYTEK radiometers, respectively.

Table 3
Mean and standard deviation values of the emissivities measured in the BS, M and VG fields

Radiometer	Spectral band (µm)	BS site	M site	VG site
CIMEL	8–13	0.957±0.007	0.974±0.011	0.982±0.007
	12.0	0.979±0.006	0.979±0.008	0.983±0.007
	10.8	0.964±0.007	0.968±0.010	0.975±0.007
	8.8	0.916±0.009	0.952±0.016	0.963±0.009
EVEREST	8–14	0.944±0.023	0.951±0.016	0.976±0.008
RAYTEK MID	8–14	0.953±0.009	0.953±0.016	0.965±0.009

The surface radiometric temperatures of each transect, measured 15 min before and after satellite overpass, were examined. The averaged and standard deviation values were calculated. To have a representative dataset of the field considered, transect measurements were carried out at regular steps (5 m in BS and M site, and 10 m in VG). Three different paths were considered according to the solar plane: one in parallel, another in perpendicular and the last in diagonal. With this strategy, we wanted to avoid too many measurements over samples with sunlit soil.

As the brightness temperatures over the mixed and vegetation surface regimes were observed to be highly variable, only the measurements falling with the 1-sigma limits were used for these locations (M and VG values in Fig. 3). The aim of the transects was to characterize 3 different regimes, a pure bare soil, a pure green vegetation and a mixed surface. The high variable values observed in vegetated and mixed surfaces showed that some measurements were probably made including a small clean area of bare soil, with a temperature not representative of the surface considered. With the 1-sigma limit, more than 68% of the measurements were considered and the measurements due to these bare soil areas could be rejected. On the contrary, bare soil depicted less variability in terms of temperature, thus all measurements were used in the retrieval of the brightness temperature for this regime (BS values in

Table 4
Coordinates and brightness temperatures of the pixel grid from AATSR spectral bands centered at 11 µm and 12 µm with both nadir and forward view angles

Pixel	Latitude (N)	Longitude (W)	T_{bt} (K) 11 µm nadir	T_{bt} (K) 11 µm forward	T_{bt} (K) 12 µm nadir	T_{bt} (K) 12 µm forward
1	31°39′59″	7°36′32″	299.97	297.42	298.54	295.56
2	31°39′51″	7°35′55″	298.95	298.84	297.62	296.96
3	31°39′43″	7°35′18″	299.59	298.84	298.27	296.96
4	31°39′36″	7°34′41″	298.07	298.92	296.86	296.92
5	31°40′30″	7°36′23″	297.08	298.49	296.05	296.56
6	31°40′23″	7°35′46″	299.09	299.61	297.87	297.69
7	31°40′15″	7°35′09″	300.46	299.61	299.20	297.69
8	31°40′07″	7°34′32″	299.66	299.34	298.44	297.41
9	31°41′02″	7°36′14″	298.64	298.94	297.43	297.08
10	31°40′55″	7°35′37″	300.33	298.78	299.04	296.98
11	31°40′47″	7°35′00″	301.80	298.78	300.43	296.98
12	31°40′39″	7°34′23″	301.56	299.16	300.30	297.37
13	31°41′34″	7°36′05″	299.55	298.85	298.30	297.05
14	31°41′26″	7°35′28″	301.36	298.31	300.06	298.52
15	31°41′19″	7°34′51″	302.14	298.31	300.85	296.52
16	31°41′11″	7°34′14″	302.56	298.98	301.26	297.17

Fig. 3). Finally the variability in the brightness temperature was represented by the standard deviation of the appropriate measurements.

3.3.2. Emissivity

The emissivity was obtained by applying the Emissivity Box Method. The box allows the retrieval of the surface emissivity from three different measurements according to:

$$\varepsilon_\lambda = \frac{B_\lambda(T_{\text{surface}}^{\text{hot cover}}) - B_\lambda(T_{\text{rad}}^{\text{blackbody}})}{B_\lambda(T_{\text{surface}}^{\text{cold cover}}) - B_\lambda(T_{\text{rad}}^{\text{blackbody}})} \tag{5}$$

where $B_\lambda(T_{\text{surface}}^{\text{cold cover}})$ is the measurement of the sample using the cold lid, $B_\lambda(T_{\text{surface}}^{\text{hot cover}})$ is the measurement of the sample using the hot lid, and $B_\lambda(T_{\text{rad}}^{\text{blackbody}})$ is the measurement of the brightness temperature of the hot lid itself.
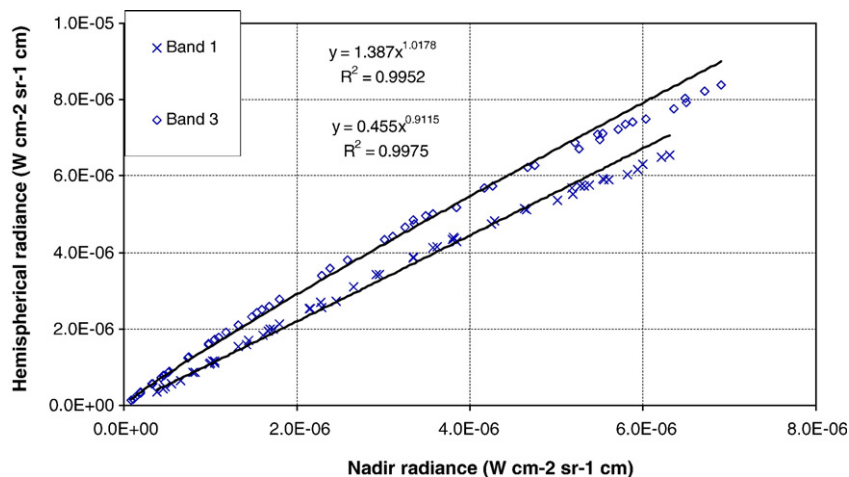

Fig. 4. Relationship between nadir and hemispherical down-welling radiance measured for both CIMEL bands 1 (8–13 µm) and 3 (10.8 µm).

The emissivity measurements were carried out in the same locations where transects were made in order to convert brightness temperature to radiometric temperature. Each radiometer for a given transect was used with the box method to retrieve emissivity over the corresponding channels. Each set of measurements was scrutinized for stability. Table 3 shows the emissivity values for the different radiometers in each site with their standard deviation obtained from both the uncertainty of the model and the measurement process. These results agree with those published in the literature (Salisbury & D'Aria, 1992).

3.3.3. Downwelling radiance and water vapor content

The downwelling radiance was measured with the CIMEL radiometer. An average value was taken from measurements within approximately 15 min before and after satellite overpass. The water vapor content was measured throughout the satellite overpass with the Microtops II photometer (Morys et al., 2001). A mean value of $W=(1.11\pm0.15)$ g cm^{-2} was obtained. A relationship between a nadir downwelling radiance and the hemispherical downwelling radiance was obtained for both CIMEL 1 and 3 spectral bands, by selecting MODTRAN simulations (Fig. 4). The simulation selection was performed according to the water vapor content over the study area at the satellite overpass. The downwelling radiance obtained through this relationship was taken into account when converting brightness temperature to radiometric temperature.

4. Satellite data

A Level 1b AATSR image of the studied area of the 5th of March 2003 10:53 UTC was used to validate the surface radiometric temperatures obtained with SW and DA algorithms. The conditions over the field site at the time of this overpass were cloud-free. The study area embraced a site of 4 by 4 pixels in the

AATSR image, with a pixel size of 1 km by 1 km (in the nadir viewing). These pixels are heterogeneous in terms of the crops contained. The geographic coordinates of the different AATSR pixels were obtained through the VISAT-BEAM program (VISualization, Analysing and processing Tool-Basic ERS & Envisat (A)ATSR and Meris Toolbox. Brockmann, 2004; Fomferra & Brockmann, 2005). These coordinates refer to the up-left latitude and longitude of each pixel. Their values as well as the brightness temperatures of the 11 µm and 12 µm bands (both in nadir and forward views) of the AATSR pixels are shown in Table 4. Table 4 shows also some pixels where forward brightness temperature is greater than the observed at nadir. This unexpected performance will be discussed in Section 6.

The algorithms proposed in Section 2 were applied to the AATSR data. Due to the application over a heterogeneous area, it was necessary to develop a method a classification based bottom up strategy for the validation of the remote sensing products using ground level measurements. With this aim in mind, a Landsat 5 image from 15 March 2003 was acquired for the same study area thanks to the WATERMED project. The conditions over the field site were also cloud-free. The Landsat image has 6 visible channels with a spatial resolution of 30 m much greater than the resolution of the AATSR ones. Therefore, for each one of the AATSR pixels studied, a minimum set of 1100 Landsat5 pixels can be overstruck (Fig. 5a). The geolocation of these data are in excellent agreement with global position system (GPS) measurements over the site, taken during the campaign.

The above mentioned Landsat 5 image was classified through a supervised maximum likelihood classification method. Three classes were taken as training endmembers for the classification process, due to the campaign strategy. They were selected as the equivalents to the sites defined in Section 3 (Bare Soil, Vegetation and Mixed site). Therefore, each pixel from the
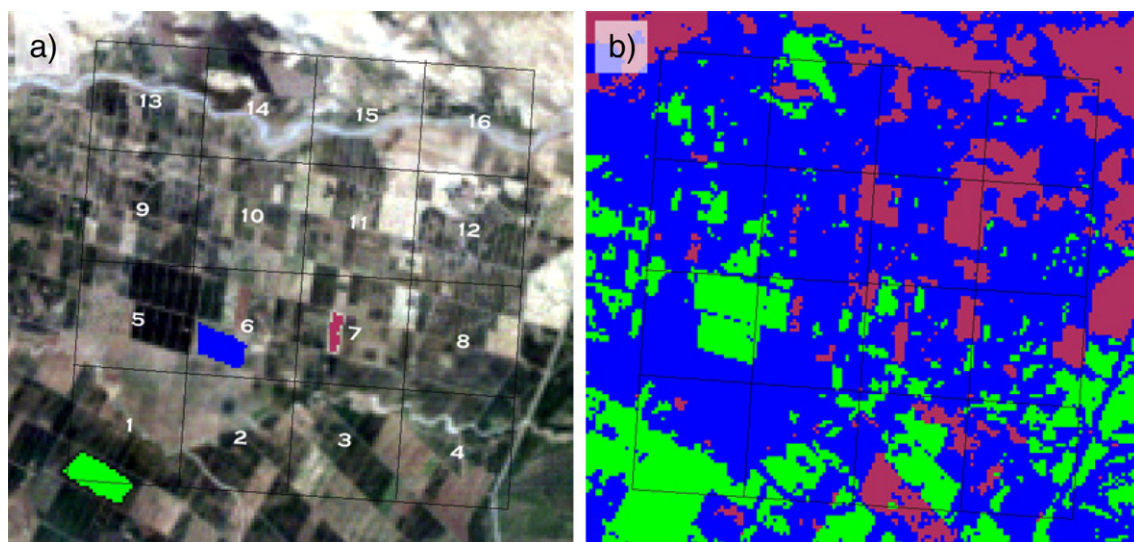

Fig. 5. a) Overstrike of the AATSR pixels considered on the Landsat 5 image and b) supervised classification image obtained from 3 endmember classes. The image was classified taking as training endmembers: bare soil (in red), green vegetation (in green) and mixed (in blue).

Table 5
Classification image from Landsat and proportions (in %) of bare soils, vegetated and mixed areas, respectively, of the AATSR pixels considered
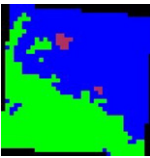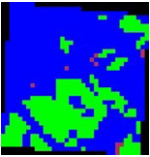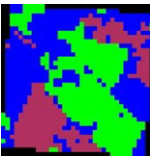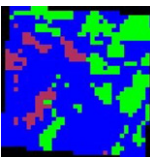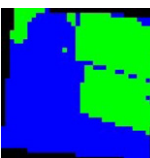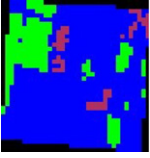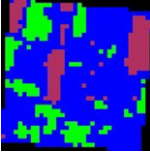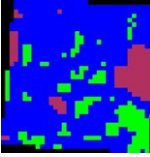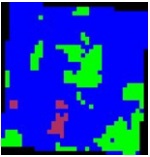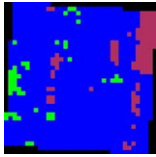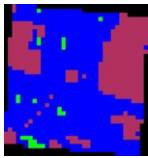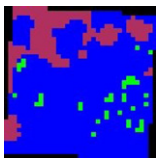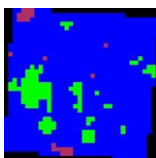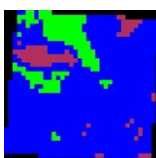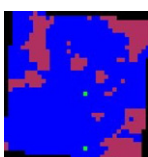
Pixel	Classification image	Proportion (%)
1		1.2 41.9 56.9
2		1.0 29.1 69.9
3		22.7 35.4 41.9
4		7.5 24.6 67.9
5		0.0 41.1 58.9
6		5.1 18.5 76.4
7		13.7 18.5 67.9
8		10.5 14.9 74.6
9		2.2 19.4 78.3

Table 5 (continued)

Pixel	Classification image	Proportion (%)
10		9.6 4.0 86.4
11		31.6 1.9 66.4
12		18.8 3.5 77.7
13		2.1 10.0 87.9
14		7.4 12.9 79.7
15		23.1 0.2 76.7
16		34.8 1.1 64.2

Landsat image was assigned to one of the three classes. The position of every AATSR pixel could be located on the Landsat5 image as both images were superimposed. This also permits to know the area covered by each AATSR pixel within the Landsat image. Fig. 5 shows a) the Landsat image with the overstrike of the AATSR pixels and b) the classification image obtained by using the three reference classes.

Our next purpose was determining the proportion of each class included within every AATSR pixel. Table 5 shows these proportions next to the area covered by the set of AATSR pixels.

5. Results

To evaluate the SW and DA algorithms we compared the surface radiometric temperature obtained from the in situ brightness measurements with the SW and DA radiometric temperature retrieved from the AATSR image on the same area. To this end the radiometric temperature for each class (see Table 6) was obtained from the radiance measured in the field ($L_\lambda^{\text{at-radiometer}}$), i. e.:

$$L_\lambda^{\text{at-radiometer}} = \varepsilon_\lambda B(\lambda, T_s) + (1 - \varepsilon_\lambda) L_\lambda^{\text{atm}\downarrow}. \quad (6)$$

Eq. (6) is obtained from Eq. (1), in which the surface level is considered, and therefore $\tau_\lambda = 1$ and $L_\lambda^{\text{atm}\uparrow} = 0$.

As shown in Sobrino et al. (1990), an effective radiometric temperature of a heterogeneous and flat surface can be obtained as $T = \Sigma P_i T_i$, where P_i is the proportion of the different surfaces considered and T_i its radiometric temperature. In our case, the effective surface radiometric temperature is $T = P_{BS}T_{BS} + P_M T_M + P_{VG}T_{VG}$, where subscripts BS, M and VG refers to Bare Soil, Mixed site and Vegetation, respectively. When the differences between the mean radiometric temperature and each one of the radiometric temperatures of the classes considered ($T_i - T \leq 15$) is less than or equal to 15 K, this averaging can be applied (Becker et al., 1981). Therefore, a mean surface radiometric temperature value for each AATSR pixel was obtained from the radiometric temperatures of Table 6 by weighting the proportions of each class in every AATSR pixel.

Finally, Table 7 shows the comparison between the surface radiometric temperature retrieved from satellite data and the surface radiometric temperature obtained from the in situ measurements. This comparison was carried out initially for a grid of 3×3 pixels centered in the areas of reference. Subsequently, the comparison was extended to a larger grid of 4×4 pixels, including some surrounding area, in order to test any spatial dependence of the results.

The results confirmed some facts observed in the simulation process: in general, RMSE in split-window algorithms decreases as more inputs parameters are explicitly included in the algorithm Thus, the RMSE decreases from 2.8 to 1.6 K. However, SW2 algorithm has an RMSE 0.3 K greater than SW1. Moreover, dual-angle algorithms have a worse behavior than the split-window ones for all the set of algorithms.

6. Discussion

In this paper, 12 algorithms based on the radiative transfer equation and considering different input parameters as ε_n, ε_f, and W are proposed. The calibration was made using simulated data. The results show that the RMSE in the temperature

Table 6
Averaged values of the surface radiometric temperature measured on the 5th of March 2003

Date	Overpass (UTC)	Surface radiometric temperature		
		BS site (°C)	M site (°C)	VG site (°C)
05/03/03	10:53	36.0±1.5	34.1±2.7	22.5±1.4

Table 7
Algorithms evaluation considering 2 different pixel grids, 4×4 and 3×3 (pixels 1, 2, 3, 5, 6, 7, 9, 10 and 11), and a window averaging filter of 2×2 pixels

Algorithm	4×4 grid			3×3 grid			2 pixel average		
	Bias, (K)	σ, (K)	RMSE (K)	Bias, (K)	σ, (K)	RMSE (K)	Bias, (K)	σ, (K)	RMSE (K)
SW1 n: quad	−2.2	1.2	2.5	−2.0	1.4	2.4	−1.2	1.0	1.5
SW2 n: quad, ε	−2.5	1.2	2.8	−2.3	1.4	2.7	−1.5	0.9	1.8
SW3 n: quad, ε, $\Delta\varepsilon$	−1.8	1.2	2.1	−1.6	1.4	2.1	−0.7	0.9	1.1
SW4 n: (W), ε, $\Delta\varepsilon$, W	−1.5	1.2	1.9	−1.3	1.4	1.9	−0.4	0.9	1.0
SW5 n: quad, ε, $\Delta\varepsilon$, W	−1.3	1.2	1.8	−1.1	1.4	1.8	−0.3	0.9	0.9
SW6 n: quad (W), ε, $\Delta\varepsilon$, W	−1.1	1.2	1.6	−0.9	1.4	1.7	−0.1	0.9	0.9
DA1 (11): quad	−1.2	3.6	3.8	−2.0	3.15	3.7	1.7	3.1	3.6
DA2 (11): quad, ε	−1.6	3.8	4.1	−2.4	3.36	4.1	1.5	3.3	3.6
DA3 (11): quad, ε, $\Delta\varepsilon$	−1.5	3.8	4.1	−2.3	3.37	4.1	1.6	3.3	3.7
DA4 (11): (W), ε, $\Delta\varepsilon$, W	−1.6	3.8	4.1	−2.4	3.52	4.2	1.5	2.9	3.2
DA5 (11): quad, ε, $\Delta\varepsilon$, W	−1.2	4.3	4.4	−2.2	3.77	4.4	2.1	3.6	4.2
DA6 (11): quad (W), ε, $\Delta\varepsilon$, W	−1.8	4.1	4.4	−2.5	3.95	4.7	1.5	0.8	1.7

Bias is the mean value of the differences between the radiometric temperatures retrieved from satellite data and the ground measured. σ is the standard deviation of these differences and RMSE is the root mean square error (all variables in K).

retrieval decrease when water vapor is considered. A negative bias was observed for both SW and DA algorithms; this means an underestimation of the LST.

A worse performance of dual-angle algorithms was found for our validation exercise. Accuracy of georegistration of AATSR pixels, and eventually resampling methods could be a source of this behavior: a misregistration of 100 m can introduce a bias of about 1.3 K if the pixel is shared 50–50% by vegetation and bare soil.

Errors due to pointing problems of the AATSR sensor and its point spread function were considered. In order to minimize the co-registration errors, we applied a procedure described in Huang et al. (2002). A spatial aggregation process was carried out over the AATSR data using a window filter of 2 by 2 pixels to twice their dimensional pixel size. The last column of Table 7 shows that, when the averaging process was carried out, the results were improved from 1.6 to 0.9 K for the best of the split-window algorithm.

The lower performance of the dual-angle algorithms was supposed to be due to the surface heterogeneity, which had a greater impact on these algorithms than on the split-window ones. Three possible sources of this performance were explored.

First, the algorithms were applied to two different pixel grids, 3×3 and a larger grid of 4×4. Results on the validation of split-window algorithms by the two grids showed that these algorithms were not dependent on the size of the area considered. Thus, although for a given pixel grid size, the
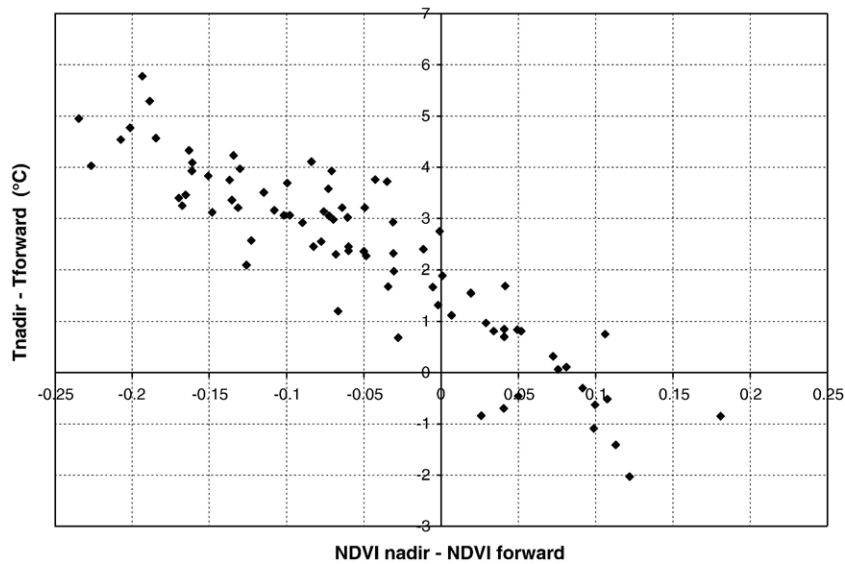
Fig. 6. Plot of the brightness temperature difference between nadir and forward views for AATSR channel 2 (centered on the 11 μm) versus nadir-forward NDVI differences.

RMSE was different for each one of the 6 split-window algorithms considered; their behavior was similar for both grids. We can apply them for areas greater than the corresponding to an AATSR pixel.

Another possible source of error included changes in surface type between the AATSR overpass (5th of March 2003) and acquisition of the Landsat image (15th of March 2003) due to harvesting, but no major harvesting event was observed to take place between these two dates.

After an analysis of the AATSR data, the foremost reason for the relatively large temperature discrepancies returned by the DA algorithm was explored. The algorithms obtained by DA method considered the effect of viewing each point of the Earth's surface from two different view-angles, one at nadir and another one at 55 degrees, and so they incorporated the angular effects due to variation of the emissivity, water vapor content and brightness temperature with view angle. But this method supposed that the surfaces observed at different angles were comparable, an assumption that is not always reliable. In the AATSR images, nadir pixels have a nominal size of 1 km × 1 km; instead of this, forward pixels have a size of 1.5 km × 2 km (according to the sensor specifications, AATSR Handbook, 2000–2002). When AATSR data are processed from Level 0 product to Level 1b product, pixels are re-gridded onto a regular grid of a nominal pixel size of 1 km × 1 km, therefore, values of some pixels are allocated according to values of neighbor pixels.

In the split-window method, pixels from two different bands that have the same spatial area are used. In the case of the dual-angle method, it is combined information from a pixel of 1 km × 1 km with another of 1.5 km × 2 km. This different pixel size was a negligible effect when evaluating DA algorithms in sea or homogeneous surfaces because, in this case, it is not so important to distinguish the value of a pixel from the nearest one. However, this effect is a critical issue in heterogeneous surfaces. It is of principal importance to know the area of each pixel; a forward pixel should cover the same area than the nadir pixel, instead, forward pixel embrace areas from the neighboring nadir pixels. Fig. 6 displays this effect.

Fig. 6 plots the brightness temperature difference between nadir and forward views for AATSR channel 2 (centered on the 11 μm) versus nadir-forward NDVI (Normalized Difference Vegetation Index) differences. The NDVI was calculated by using the AATSR reflectances of channel 5 (centered in 0.87 μm) and channel 6 (centered in 0.67 μm).

Negative values on x axis correspond to areas of higher vegetation proportion in forward than in nadir views. This implies that nadir image presents a higher proportion of soil (higher brightness temperature) than the forward image. This behavior would be in accordance with the observation geometry of the crops and are logical for incomplete canopies. As a consequence, for these areas, T_{nadir} is higher than $T_{forward}$. It should be noticed that, as observed in Table 4 where some pixels had a forward brightness temperature greater than the observed at nadir, some negative differences of brightness temperature appear in Fig. 6. These values mean that we are observing more bare soil surface (less NDVI) in forward view than in nadir view, which cannot be explained considering the geometry of the crops.

However, these values can be obtained for situations where the observation area for a pixel does not match in forward and nadir views. Hence, forward view pixel will be contaminated by bare soil surface that does not appear in the nadir pixel. This could be due to the process of re-gridded to a 1 km × 1 km size of the forward pixels when Level 1b and Level 2 AATSR products are created. This effect can also appear in the x-axis negative value pixels, but it is difficult to distinguish from the effect of the observation geometry of the crops exposed previously.

7. Conclusions

In this paper, split-window and dual-angle algorithms for surface temperature determination using AATSR data were proposed. These algorithms were calibrated over a database simulated from both MODTRAN and spectral libraries. Moreover, a methodology to validate AATSR radiometric temperatures in heterogeneous sites was proposed. In this methodology, a classification was performed over a Landsat 5 image by a supervised maximum likelihood classification method. This method made use of different well-defined classes. To carry out the evaluation of the radiometric temperatures obtained from AATSR data in heterogeneous surfaces, a Landsat image as temporally close as possible to the AATSR image was used. An analysis of the georegistration information between both platforms was carried out to make the overstrike of the images as precise as possible.

A thorough comparison using ground-truth data shows that the radiometric temperatures can be obtained from AATSR data on heterogeneous surfaces with an RMSE better than 1.7 K. This is the case of the split-window algorithm proposed that require the knowledge of more inputs. The performances of the algorithms might be lower when applied over regions with larger atmospheric water vapor contents (especially above 3 g cm^{-2}).

Although the dual-angle algorithms can probably provide more accurate retrieval of radiometric temperatures than the split-window ones (Sobrino et al., 2004), this is not the case when the satellite observes heterogeneous surfaces as it is shown in this paper.

Radiometric temperatures obtained from DA algorithms may have worse accuracy due to their dependence on the heterogeneity of the surface than SW algorithms, as the nadir–nadir proposed in this paper. For incomplete canopies, the proportion of vegetation in relation to bare soil showed in a forward-view image is greater than the proportion showed in the nadir-view one. However, situations were observed where the proportion of bare soil increases in the forward-view images. Some possibilities were considered in the interpretation of this behavior. The most likely explanation chosen for this discrepancy are the unequal pixel sizes between forward and nadir view that DA algorithms combine, due to the process where forward pixels of an AATSR image are rescaled from a spatial resolution of 1.5 km × 2 km to the same resolution of the nadir view (1 km × 1 km).

This different pixel size was not so important when retrieving surface radiometric temperature from sea or homogeneous land, but it shows to be a critical issue when we attempt to apply DA to heterogeneous land.

Thus, it is very difficult to evaluate the proportion of each class in the same pixel, and therefore this DA method cannot be operatively applied in this direction. We consider that if additional information is supplied about the geographic location of the forward pixel corners, it would be possible to identify the area covered by the pixel and a proper DA algorithm would be applied. We suggest the consideration of this footprint problem for the design of future multiangular sensors. It should be noticed that, a possible source of error in the behavior of DA algorithms could be the fact that forward view images were used, but the classification process was performed over a nadir-view image (Landsat image). A good possibility in the future could be to apply the proposed supervised classification method over higher resolution images with the same view angle than the AATSR forward images, like for example the images obtained from the CHRIS/PROBA satellite. The authors are working on this matter. Further studies are necessary to evaluate the behavior of the DA algorithms in heterogeneous surfaces.

References

Abreu, L. W., & Anderson, G. P. (Eds.). (1996). *The MODTRAN 2/3 Report and LOWTRAN 7 Model, Modtran Rep., Contract F19628-91-C-0132, Phillips Lab., Hanscom Air Force Base, Massachussets*.

Barton, I. J. (1992). Satellite-derived sea surface temperatures: A comparison between operational, theoretical and experimental algorithms. *Journal of Applied Meterology*, *31*, 432−442.

Becker, F. (1987). The impact of spectral emissivity on the measurement of land surface temperature from a satellite. *International Journal of Remote Sensing*, *8*(10), 1509−1522.

Becker, F., & Li, Z. -L. (1990). Temperature-independent spectral indices in thermal infrared bands. *Remote Sensing of Environment*, *32*, 17−33.

Becker, F., Ngai, W., & Stoll, M. P. (1981). An active method for measuring thermal infrared effective emissivities—Implications and perspectives for remote sensing. *Advances in Space Research*, *1*(10), 193−210.

Berk, A., Bernstein, L. S., Anderson, G. P., Acharya, Robertson, D. C., Chetwynd, J. H., & Adler-Golden, S. M. (1998). MODTRAN cloud and multiple scattering upgrades with application to AVIRIS. *Remote Sensing of Environment*, *65*, 367−375.

Brockmann, C. (2004). Demonstration of the BEAM software — A tutorial for making best use of VISAT. *Proc. MERIS User Workshop, ESA SP-549, May 2004*.

Buettner, K. J. K., & Kern, C. D. (1965). The determination of infrared emissivities of terrestrial surfaces. *Journal of Geophysical Research*, *70*, 1329−1337.

Caselles, V., & Sobrino, J. A. (1989). Determination of frosts in orange groves from NOAA-9 AVHRR data. *Remote Sensing of Environment*, *29*, 135−146.

Chédin, A., Scott, N. A., & Berroir, A. (1982). A single-channel double-viewing angle method for sea surface temperature determination from coincident METEOSAT and TIROS-N radiometric measurements. *Journal of Applied Meterology*, *21*, 613−618.

Dana, R. W. (1969). *Measurement of 8–14 micron emissivity of igneous rocks and mineral surfaces.* NASA Science Report NSG-632 Greenbelt, MD: Goddard Space Flight Center.

Dorman, J. L., & Sellers, P. J. (1989). A global climatology of albedo, roughness length, and stomatal resistance for atmospheric general circulation models as represented by the simple biosphere model (SiB). *Journal of Applied Meteorology*, *28*, 833−855.

Estelles, V., Utrillas, M. P., Martinez-Lozano, J. A., Alcantara, A., Alados-Arboledas, L., Olmo, F. J., et al. (2004). Aerosol related parameters

intercomparison of Cimel sunphotometers in the frame of the VELETA2002 field campaign. *Optica Pura y Aplicada*, *37*(3), 3289−3297.

Fomferra, N., & Brockmann, C. (2005). *Beam—The ENVISAT MERIS and AATSR Toolbox*. MERIS AATSR Workshop. ESRIN, 26–30 September 2005.

Gómez-Amo, J. L., Martínez-Lozano, J. A., Utrillas, M. P., Pedrós, R., & Estellés, V. (2006). Column-integrated aerosol optical properties in Sodankyla (Finland) during the Solar induced Fluorescence Experiment (SIFLEX-2002). *Journal of Geophysical Research*, *111*, D05202. doi:10.1029/2005JD006051

Grant, W. B. (1990). Water vapor absorption coefficients in the 8–13 mm spectral region: A critical review. *Applied Optics*, *29*, 451−462.

Huang, C., Townshend, J. R. G., Liang, S., Kalluri, S. N. V., & DeFries, R. S. (2002). Impact of sensor's point spread function on land cover characterization: Assessment and deconvolution. *Remote Sensing of Environment*, *80*, 203−212.

Jacob, F., Petitcolin, F., Schmugge, T., Vermote, E., French, A., & Ogawa, K. (2004). Comparison of land surface emissivity and radiometric temperature derived from MODIS and ASTER sensors. *Remote Sensign of Environment*, *90*, 137−152.

Jia, L., Li, Z. -L., Menenti, M., Su, Z., Verhoef, W., & Wan, Z. (2003). A practical algorithm to infer soil and foliage component temperatures from bi-angular ATSR-2 data. *International Journal of Remote Sensing*, *24*, 4739−4760.

Labed, J., & Stoll, M. P. (1991). Spatial variability of land surface emissivity in the thermal infrared band: Spectral signature and effective surface temperature. *Remote Sensign of Environment*, *38*, 1−17.

Lagouarde, J. P., Kerr, Y. H., & Brunet, Y. (1995). An experimental study of angular effects on surface temperature for various plant canopies and bare soils. *Agricultural and Forest Meteorology*, *77*, 167−190.

McAtee, B. K., Prata, A. J., & Lynch, M. J. (2003). The angular behavior of emitted thermal infrared radiation (8–12 μm) at a semiarid site. *Journal of Applied Meteorology*, *42*(8), 1060−1071.

Moré, J. J. (1997). The Levenberg–Marquardt algorithm: Implementation and theory. In G. A. Watson (Ed.), *Numerical AnalysisLecture notes in mathematics*, *Vol. 630*. (pp. 105−106) : Springer Verlag.

Morys, M., Mims, F. M., III, Hagerup, S., Anderson, S. E., Baker, A., Kia, J., et al. (2001). Design, calibration, and performance of MICROTOPS II handheld ozone monitor and Sun photometer. *Journal of Geophysical Research*, *106*, 14,573−14,582.

Nerry, F., Labed, J., & Stoll, M. -P. (1990). Spectral properties of land surfaces in the thermal infrared 2. Field method for spectrally averaged emissivity measurements. *Water Resources Research*, *95*(B5), 7045−7054.

Prata, A. (2002). *Land surface temperature measurement from space: AATSR algorithm theoretical basis document*.

Prata, A. J. (1993). Land surface temperatures derived from the AVHRR and ATSR, 1 Theory. *Journal of Geophysical Research*, *89D9*, 16689−16702.

Press, W. H., Flanery, B. P., Teukolsky, S. A., & Vetterling, W. T. (1989). *Numerical recipes*. Cambridge, UK: Cambridge University Press.

Price, J. C. (1984). Land surface temperature measurements from the split window channels of the NOAA-7 AVHRR. *Journal of Geophyical Research*, *79*, 5039−5044.

Salisbury, J. W., & D'Aria, D. M. (1992). Emissivity of terrestrial materials in the 8–14 μm atmospheric window. *Remote Sensing of Environment*, *42*, 83−106.

Schmugge, T., French, A., Ritchie, J. C., Rango, A., & Pelgrum, H. (2002). Temperature and emissivity separation from multispectral thermal infrared observations. *Remote Sensing of Environment*, *79*, 189−198.

Scott, N. A., & Chedin, A. (1981). A fast line by line method for atmospheric absorption computations: The automatized atmospheric absorption atlas. *Journal of Applied Meteorology*, *20*, 802−812.

Smith, D. L., Delderfield, J., Drummond, D., Edwards, T., Mutlow, C. T., Read, P. D., et al. (2001). Calibration of the AATSR instrument. *Advances in Space Research*, *28*(1), 31−39.

Sobrino, J. A., & Caselles, V. (1993). A field method for measuring the thermal infrared emissivity. *ISPRS Journal of Photogrammetry and Remote Sensing*, *48*, 24−31.

Sobrino, J. A., Caselles, V., & Becker, F. (1990). Significance of the remotely sensed thermal infrared measurements obtained over a citrus orchard. *ISPRS Journal of Photogrammetry and Remote Sensing*, *44*, 343−354.

Sobrino, J. A., Coll, C., & Caselles, V. (1991). Atmospheric corrections for land surface temperature using AVHRR channel 4 and 5. *Remote Sensing Environment*, *38*, 19−34.

Sobrino, J. A., & Cuenca, J. (1999). Angular variation of thermal infrared emissivity for some natural surfaces from experimental measurements. *Applied Optics*, *38*, 3931−3936.

Sobrino, J. A., El-Kharraz, J., & Li, Z. -L. (2003). Surface temperature and water vapour retrieval from MODIS data. *International Journal of Remote Sensing*, *24*, 5161−5182.

Sobrino, J. A., Li, Z. -L., Stoll, M. P., & Becker, F. (1994). Improvements in the split-window technique for the land surface temperature determination. *IEEE Transactions on Geoscience and Remote Sensing*, *32*(2), 243−253.

Sobrino, J. A., Li, Z. -L., Stoll, M. P., & Becker, F. (1996). Multi-channel and multi-angle algorithms for estimating sea and land surface temperature with ATSR data. *International Journal of Remote Sensing*, *17*, 2089−2114.

Sobrino, J. A., & Raissouni, N. (2000). Toward remote sensing methods for land cover dynamic monitoring: Application to Morocco. *International Journal of Remote Sensing*, *21*(2), 353−366.

Sobrino, J. A., Raissouni, N., Olioso, A., Hasager, C. B., Ait Belaid, M., Abdel Rahman, S., et al. (2001). WATERMED — WATer use Efficiency in natural vegetation and agricultural areas by Remote sensing in the MEDiterranean basin. *IGARSS, IEEE Intern. Geos. And Rem. Sens. Symp.* Sydney, Australia: University of New South Wales.

Sobrino, J. A., Raissouni, N., Simarro, J., Nerry, F., & Petitcolin, F. (1999). Atmospheric water vapor content over land surfaces derived from the AVHRR data: Application to the Iberian Peninsula. *IEEE Transactions on Geoscience and Remote Sensing*, *37*, 1425−1434.

Sobrino, J. A., Sòria, G., & Prata, A. J. (2004). Surface temperature retrieval from Along Track Scanning Radiometer 2 data: Algorithms and validation. *Journal Geophysical Research*, *109*, D11101. doi:10.1029/2003JD004212

Wan, Z., & Dozier, J. (1989). Land-surface temperature measurement from space: Physical principles and inverse modeling. *IEEE Transactions on Geoscience and Remote Sensing*, *27*, 268−278.